Title: Methane oxidation dynamics in a karst subterranean estuary

Authors: David Brankovits[a,b,1,*] and John W. Pohlman[b]

[a] Department of Marine Biology, Texas A&M University at Galveston, Galveston, TX 77553, USA;

[b] U.S. Geological Survey, Woods Hole Coastal and Marine Science Center, Woods Hole, MA 02543, USA;

[1] Present address: Department of Marine Chemistry and Geochemistry, Woods Hole Oceanographic Institution, Woods Hole, MA 02543, USA;

*corresponding author

Email addresses: D.B. (dbrankovits@whoi.edu), J.W.P. (jpohlman@usgs.gov)

ABSTRACT

Chemical gradients between fresh, brackish and saline waters shape biogeochemical reactions and organic matter transformation within subterranean estuaries. In the Yucatán Peninsula's karst subterranean estuary (KSE), methane and dissolved organic matter generated during the anaerobic decomposition of tropical forest vegetation are transported into flooded cave networks where microbial consumption greatly reduces their discharge to the coastal ocean. To test the hypothesis that chemoclines associated with salinity gradients of the KSE are sites of methane oxidation, we obtained methane concentration and $\delta^{13}C$ profiles of unprecedented vertical resolution from within a fully-submerged cave system located 6.6 km inland from the coastline using the 'OctoPiPi' (OPP) water sampler. Along a 12-24 cm thick low-salinity-halocline at ~4.5 m water depth, salinity increased from 0.2 to 1.8 psu, methane concentrations decreased, and $\delta^{13}C$ values became more positive, as expected for microbial methane oxidation. By contrast, as salinity increased from 1.8 to 36 psu through a 24-36 cm thick high-salinity-halocline between the meteoric lens and the saline groundwater at ~20 m water depth, methane concentrations and $\delta^{13}C$ values were constant. Conservative mixing and kinetic isotope models incorporating the methane data confirm a hotspot for microbial methane oxidation at the low-salinity-halocline. At least 98% of methane originating in the anoxic fresh waters was removed before its transport via channelized flow towards the coastline. These data provide novel insight into the spatial constraints of methane dynamics and organic matter transformation within a karst subterranean estuary.

INTRODUCTION

Density stratified coastal aquifers are highly structured aquatic environments with sharp physicochemical gradients that affect organic matter cycling (Kroeger and Charette, 2008; Moore, 2010; Santoro, 2010; Schutte et al., 2016). Analogous transitional zones are found in estuaries (Chanton and Lewis, 1999), hydrothermal vents (Corliss et al., 1979; Paull et al., 1984), deep-sea cold seeps (Levin, 2005), and meromictic (permanently stratified) lakes (Bastviken et al., 2008). The exchange of material across these ecotones creates biogeochemical hotspots that also shape the biological communities inhabiting them. Similar processes occur where meteoric fresh water mixes with marine-derived groundwater in karst (eroded carbonate) aquifers (Pohlman, 2011), also referred to as karst subterranean estuaries (KSEs). Because nutrient transport and elemental cycling along many coastlines are influenced by material exported from subterranean estuaries via submarine groundwater discharge (Kwon et al., 2014; Moore, 2010; Santoro et al., 2008), investigating the transformation of organic matter associated with density stratification within these habitats may provide insight into an important component of the coastal ocean carbon cycle.

The mixing of energy-yielding organic compounds (electron donors) with electron accepting agents of cellular respiration across salinity-dominated density interfaces (pycnoclines) impacts the transformation of organic matter, including the greenhouse gas methane, in aquatic ecosystems. In meromictic lakes and reservoirs where water masses are permanently stratified, 20-60% of the organic carbon produced in surface waters is transported to the anoxic hypolimnion (Bastviken et al., 2008). A fraction of this carbon is transformed into methane (CH_4) by sedimentary or water column methanogenesis (Wetzel, 2001). The methane is either oxidized and returned to the lake's carbon cycle (Bastviken et al., 2004) where it has been shown to contribute carbon and energy to the limnic food web (Bastviken et al., 2003; He et al., 2015), or it may transfer to the atmosphere (Bastviken et al., 2011) where it is a greenhouse gas 25 times more potent than carbon dioxide on a 100-year time scale (IPCC, 2014).

Hydrogeological conditions in highly permeable carbonate platforms limit mixing, which creates a meromictic condition allowing meteoric freshwater to permanently override marine-derived saline groundwater (Beddows et al., 2007; van Hengstum et al., 2011). These coastal areas frequently contain dissolutional karst features, such as sinkholes and cave passages (Ford and Williams, 2013), with caves playing an important role in the seaward transport of dissolved materials (Bauer-Gottwein et al., 2011; Beddows et al., 2002; Kovacs et al., 2017; Menning et al., 2015). Because karst coastlines account for 25% of the global coastal geomorphology (Ford and Williams, 2013) and 12% of volumetric estimates for global submarine groundwater discharge (Beck et al., 2013), caves may be an important conduit for transmitting terrestrial material to the oceans globally.

Numerous studies have characterized the hydrogeology (Beddows et al., 2007; Coutino et al., 2017; Kambesis and Coke, 2013; Perry et al., 2002) and invertebrate zoology (Alvarez et al., 2015; Humphreys, 1999; Iliffe and Kornicker, 2009) associated with the salinity mixing zone (halocline) between the meteoric lens and saline groundwater in KSEs. Biogeochemical studies suggest organic matter degradation and associated cycling of nitrogen and sulfur species are enhanced at the meteoric-saline halocline in sinkholes and interior caves (Humphreys, 1999; Pohlman, 2011; Socki et al., 2002). High-resolution vertical sampling across the salinity gradient of an eutrophic open sinkhole revealed changes in the chemistry and microbiology (Seymour et al., 2007). However, a similar approach has not been applied to characterize the cycling of carbon along chemoclines that occur within the flooded oligotrophic caves.

The Yucatán Peninsula's 165,000 km^2 carbonate platform contains vast networks of cave passages (Kambesis and Coke, 2013) flooded by the subterranean estuary. The environment supports a rich community of anchialine fauna (Iliffe and Kornicker, 2009; Stock et al., 1986) consisting primarily of cave-adapted crustaceans (Alvarez et al., 2015) that are specifically adapted to the oligotrophic environment (Bishop et al., 2015; Iliffe and Kornicker, 2009; Stock et al., 1986). Methane and other forms of dissolved organic matter formed from decomposed vegetation that is assimilated by microbes are

an important carbon and energy source for the food web (Brankovits et al., 2017). The water column in these flooded caves is characterized by distinct fresh-, brackish- and saline-water layers, limited particulate organic matter, and high concentrations of dissolved organic matter in the freshwater portion of the water column.

In this study, we test the hypothesis that methanotrophy occurs at the anoxic-hypoxic interface between the fresh and brackish water layers in the meromictic coastal aquifer of the Yucatán Peninsula's karstic platform. A high-resolution water sampling device developed for this study was used to obtain pristine cm-scale vertical chemical profiles across haloclines within cave passages of the KSE. Concentrations and stable carbon isotopic values of methane collected along the full salinity spectrum were used to construct conservative mixing and kinetic isotope models to differentiate changes in concentrations and carbon isotope ratios imposed by physical mixing between water masses from those caused by microbial production and consumption of methane. Methane plays a prominent role in ecosystem dynamics (Bastviken et al., 2003; Deines et al., 2009; DelVecchia et al., 2016; Devlin et al., 2015; Grey, 2016), the global carbon cycle (Bastviken et al., 2011; Boetius and Wenzhofer, 2013) and the atmospheric greenhouse gas inventory (IPCC, 2014; Reeburgh, 2007). This study has the potential to define how methane dynamics within KSEs influence anchialine ecosystems and remove methane from the groundwater prior to its expulsion into the coastal ocean, evasion into overlying tropical soils, and, ultimately, the atmosphere.

MATERIALS AND METHODS

Study sites and sampling periods

Field campaigns were conducted in January 2015 and January 2016 in flooded caves accessed through the Cenote Bang sinkhole (20˚ 12.62' N 87˚ 30.064' W). Cenote Bang is part of the Ox Bel Ha cave system (with >240 km mapped cave passages) that underlays a seasonally dry tropical forest south of Tulum, Quintana Roo, Mexico (Fig. 1a-b). This region is located on the Caribbean coast of the Yucatán Peninsula where the low elevation karst terrain lacks surface streams and rivers due to the high

permeability of the limestone bedrock (e.g., Beddows et al., 2007; Perry et al., 2002). Here, abundant cave passages are found in the KSE over a substantial area (Bauer-Gottwein et al., 2011; Kambesis and Coke, 2013). Cenote Bang provides access to a complex meromictic subterranean aquatic environment with a shallow (<4.5 m) meteoric fresh water (FW) layer (<0.5 psu), an intermediate (4.5-20 m) meteoric brackish water (BW) layer (0.5-30.0 psu), and deep (>20 m) saline groundwater (SG) (30.0-35.0 psu) (Fig. 1c) (Brankovits et al., 2017). Here, the salinity/density interface between the FW and BW is referred to as the low-salinity-halocline and the interface between the BW and SG is referred to as the high-salinity-halocline. Although hydrological conditions are seasonally dynamic which may affect halocline thickness, these water masses remain stratified year-round (Brankovits et al., 2018). In both years, sampling was conducted during the dry season which typically lasts from December to April/May (Curtis et al., 1996; Kottek et al., 2006). Dissolved oxygen concentrations were lower in the BW in 2016 than they were 2015 (Fig. 1d). The caves investigated in this study had no visible evidence of direct or indirect human alterations; therefore, they are presumed to represent a pristine habitat.

Sample collection and processing

Sampling was carried out on SCUBA, following diving and safety protocols established by the American Academy of Underwater Sciences and the National Speleological Society-Cave Diving Section. Water samples were obtained at cm-scale vertical resolution across the low-salinity- and high-salinity-haloclines using the OctoPiPi (OPP) water sampling system developed by the U.S. Geological Survey (USGS) (Fig. 2). The OPP samplers used in this study consist of a rack of ten 60 ml plastic syringes mounted and evenly distributed along an aluminum frame with a mechanical, spring-powered trigger-system that fills syringes when activated. An OPP with fixed 12 cm syringe spacing (Fig. 2) and another with 2.5 cm syringe spacing (the mini-OPP) were deployed during this study. The OPPs were mounted vertically across interfaces identified from depth-salinity profiles collected prior to deployment and

150 visually confirmed during deployment (Fig. 1c). The OPPs were left in place for at least
151 24 hr to allow the water column to re-stratify before being triggered. The top-mount of
152 the OPP was connected to either an inflated dive lift bag or elastic bands carefully
153 attached to the cave ceiling. The bottom-mount was connected to 1/8" braided nylon line
154 deployed by dive reel and attached to at least 5 kg of lead for stability. When triggered,
155 the OPP slowly and simultaneously filled the syringes to a volume of 40-60 ml
156 depending on OPP geometry. The 60-ml syringes were fitted with 3-way stopcocks that
157 were closed immediately after triggering to contain the samples. Prior to deployment, the
158 syringe assemblies were rinsed thoroughly with distilled water and completely dried.
159 Following OPP recovery, the syringes were transported on ice to the field lab,
160 where they were processed within eight hours of collection following protocols
161 described by Brankovits et al. (2017). Briefly, the 60-ml water sample was divided into
162 subsamples for further geochemical analyses of dissolved constituents, including, but not
163 limited to, methane, dissolved inorganic carbon, dissolved organic carbon, inorganic
164 nutrients and ions. For the present study, chloride and sulfate ion concentrations as well
165 as methane concentrations and $\delta^{13}C$ values are reported. Samples for ion analysis were
166 filtered through a 0.45 µm Acrodisc® syringe filter and collected in a 2-ml plastic
167 screw-top vial. 30-ml serum vials for methane water samples were prepared prior to
168 sample collection by adding 0.5 ml 8 M NaOH into the empty vial as a preservative,
169 sealing the container with 1 cm thick butyl septa, and vacating the vial of air with a
170 vacuum pump. An unfiltered 20-ml water sample was then transferred from the syringe
171 into the serum vial by piercing the septum with a 20-gauge syringe needle and regulating
172 water flow with the stopcock. Water samples were stored in the fridge at 7 °C.
173
174 *Geochemical analysis*
175 Geochemical analyses were performed at the Woods Hole Oceanographic
176 Institution (WHOI) and USGS in Woods Hole MA, USA. After balancing the headspace
177 of the serum vial for methane analysis to 1 atmosphere with helium, headspace methane
178 concentrations were determined using a Shimadzu 14-A gas chromatograph (GC)

equipped with a flame ionization detector (FID). The gases were isothermally (50 °C) separated with a Poraplot-Q stainless steel column (8 ft x 1/8" OD) packed with 60/80 mesh and quantified against certified gas standards with a relative standard deviation (RSD) of 2.8% or less. Headspace concentrations were converted to dissolved concentrations using an established method (Magen et al., 2014). The stable carbon isotope composition of methane ($\delta^{13}C$-CH_4) from the headspace of the serum vials was determined using a Thermo-Finnigan DELTA^{Plus} XL isotope ratio mass spectrometer (IRMS) coupled to an Agilent 6890 Gas Chromatograph (GC) via a Finnigan GCCIII combustion interface. Variable volume (1-15.0 ml) gas samples, depending on concentrations, were introduced through a gas sampling valve into a 1 ml min^{-1} He carrier gas stream. Following an established method (Popp et al., 1995) with modifications, methane and other condensable gases were trapped on fused silica capillary packed with 80/100 mesh Poraplot-Q immersed in liquid nitrogen. The gases were thermally desorbed from the column at 150 °C and separated on a 30 m, 0.32 mm ID Poraplot-Q column at −40 °C prior to being oxidized to CO_2 and analyzed by IRMS. The $^{13}C/^{12}C$ ratios of methane are expressed in the standard δ-notation using tank CO_2 referenced to the Vienna Pee Dee Belemnite (VPDB) standard. The standard deviation (1 σ) of a 1% CH_4 standard analyzed at least every 8 samples was 0.3‰.

Sulfate and chloride concentrations were determined using a Metrohm 881 Compact Plus ion chromatograph (IC) equipped with a Metrosep A Supp 5-250 anion column. Samples from the FW, BW and SG were diluted by factors of 31, 61 and 101, respectively, to maintain chloride concentrations within the range of the conductivity detector. Peak areas for sulfate and chloride were quantified against equivalently diluted International Association for the Physical Sciences of the Oceans (IAPSO) standard seawater analyzed at the beginning of the run and after every fifth sample. Chloride concentrations (mM) were converted to mg l^{-1} and multiplied by 0.0018066 to report salinity (psu). The analytical error (standard deviation) for dissolved constituents was ± 3.5% of the IAPSO (International Association for the Physical Sciences of the Oceans) standard sulfate and chloride values.

208 *Conservative mixing calculations*

209 Conservative mixing models were used to differentiate the roles of physical
210 mixing from *in situ* microbial oxidation (consumption) on the concentration and isotopic
211 composition of methane through the salinity gradient. This approach has been used to
212 investigate carbon dynamics in estuaries (Chanton and Lewis, 1999) and brine-affected
213 marine pore waters (Pohlman et al., 2008). The conservative mixing calculations were
214 conducted using salinity and methane data obtained from the OPP profiles similar to the
215 approach used by Brankovits et al. (2017) using manually collected samples. By
216 applying the mixing model to each OPP deployment, it was possible to determine the
217 fraction of methane removed by methanotrophy along gradients where high methane in
218 the FW mixes with lower methane in the BW.
219
220 *Kinetic isotope models*

221 To delineate if changes in the carbon isotope ratios were due to oxidation or
222 mixing with other methane sources, the measured $\delta^{13}C$ values and concentrations of
223 methane were incorporated into the kinetic isotope model described by Leonte et al.
224 (2017). The approach is based on the observation that isotopic fractionation during
225 methane oxidation causes the residual methane to become increasingly enriched with ^{13}C
226 relative to the source value (a.k.a., the kinetic isotope effect) (Barker and Fritz, 1981;
227 Whiticar, 1999). Coupled shifts in methane concentration and $\delta^{13}C$ values during
228 oxidation may be described with either a "closed-system" Rayleigh isotopic
229 fractionation model (Damm et al., 2007; Leonte et al., 2017) or an "open-system"
230 isotope model (e.g., Kessler et al., 2006; Leonte et al., 2017). The primary assumption of
231 the Rayleigh model is that microbial methane oxidation is the only process altering the
232 $\delta^{13}C\text{-}CH_4$ values following first-order reaction kinetics. This model assumes no mixing
233 with other methane-rich waters; however, if methane inputs from alternate sources occur
234 but are so low that the mixing does not substantially alter the $\delta^{13}C$ of the bulk methane
235 pool, the closed-system assumption remains valid (Leonte et al., 2017). By contrast, the
236 open-system model accounts for mixing of methane-rich waters with different methane

content and $\delta^{13}C$ values, in addition to the kinetic isotope effect that occurs during oxidation. By comparing each of these models to measured $\delta^{13}C$ values and concentrations of methane released from seafloor seeps in the Hudson Canyon of the U.S. Atlantic Margin, Leonte et al. (2017) were able to distinguish methane oxidation and methane dispersion from other sources. Here, we apply a similar approach to assess methane oxidation at the low-salinity-halocline (where isotopic evidence for methane oxidation was obtained).

Equations for the Rayleigh (Eq. 1) and open-system (Eq. 2) models are:

(1) $$f_c = 1 - \left(\frac{\delta R+1000}{\delta R_0+1000}\right)^{\left(\frac{\alpha_c}{1-\alpha_c}\right)}, \text{ and}$$

(2) $$f_o = \frac{\alpha_o}{1-\alpha_o}\left(\frac{\delta R_0+1000}{\delta R+1000} - 1\right),$$

where f is the fraction oxidized, α is the isotope fractionation factor, the subscripts c and o refer to the closed- and open-system models, δR_0 is the source (or initial) $\delta^{13}C\text{-}CH_4$ value of methane in the fresh water, and δR is the $\delta^{13}C\text{-}CH_4$ value at a later time. δR_0 (−67.49‰) is the average $\delta^{13}C\text{-}CH_4$ from the sample with the highest methane concentration (7,793 nM; $\delta^{13}C$ = − 67.48‰) and the lowest $\delta^{13}C$ value (−67.51‰; 7,295 nM). The average concentration for those samples (C_0) is 7,544 nM, which is used to calculate the fraction methane oxidized (see Results) as described by Leonte et al. (2017).

The isotope fractionation factors for the closed-system (α_c, Eq. 3) and open-system (α_o, Eq. 4) models were obtained through linearization of Eqns. (1) and (2):

(3) $$\text{slope}_c = \frac{\alpha_c}{1-\alpha_c}, \text{ and}$$

(4) $$\text{slope}_o = -\frac{\alpha_o C_o(\delta R_0+1000)}{1-\alpha_o},$$

where slope_c and slope_o are the slopes of the linear regressions for the two models (Fig.3). The resulting isotope fractionation factors for the closed-system model (α_c =

1.004) and open-system model (α_o = 1.024) are comparable to those from other systems (Leonte et al., 2017; Whiticar, 1999).

RESULTS

Vertical chemical profiles

High-resolution sampling of the mixing zones revealed dramatic methane and sulfate gradients associated with the shift in salinity at the shallow, low-salinity-halocline (Fig. 4). In the FW, salinity ranged from 0.17 to 0.47 psu, with the exception a single 0.92 psu salinity value in 2015. This anomalous value is likely a sample handling or analytical artifact because it is not consistent with any of the sonde measurements (Fig. 1). The FW had high methane concentrations (ranging from 1,272 to 7,793 nM) that were ^{13}C-depleted (ranging from −58.1‰ to −67.5‰). By contrast, the BW had oligohaline salinity (ranging from 1.81 to 1.88 psu) and lower methane concentrations (ranging from 37 to 132 nM) that were ^{13}C-enriched (ranging from −47.8‰ to −55.5‰) relative to the FW. The profile obtained in January 2015 had steeper chemical gradients and a substantially higher average methane concentration (7,187 ± 185 nM) and ^{13}C-depleted δ^{13}C-CH_4 value (−67.1 ± 0.2‰) than the January 2016 profile average concentration (3,246 ± 238 nM) and δ^{13}C-CH_4 value (−64.0 ± 1.3‰).

The vertical extent, or thickness, of the halocline was 12 cm in 2015 (Fig. 4a) and 24 cm in 2016 (Fig. 4b). The average depth of the halocline was 4.2 m in 2015 and 4.6 m in 2016. A higher resolution (2.5 cm) vertical profile obtained from the low-salinity-halocline with the mini-OPP provides a more detailed record of the intermediate chemical properties (Fig. 4c). Increasing salinity across the chemical gradient (from 0.74 to 1.84 psu) was associated with decreasing methane concentrations (from 1,419 to 42 nM) and increasing δ^{13}C-CH_4 values (from −65.2 to −52.0‰).

Across the deeper high-salinity-halocline, an extreme shift in salinity and sulfate concentration was observed, but the methane concentrations and δ^{13}C-CH_4 values were relatively constant (Fig. 5a-b). Salinity varied from oligohaline (as low as 1.79 psu) to mesohaline (as high as 14.38 psu) in the BW and from 31.11 to 35.95 psu in the SG.

Methane concentrations ranged from 9 to 121 nM with δ^{13}C-CH_4 values −44.6‰ to −57.5‰ throughout the profiles with no obvious trend that would imply methane consumption or production at the interface. Methane across the interface was higher in concentration (ranging from 50 nM to 121 nM) and more depleted (−50.4‰ to −57.5‰) in 2015 than in 2016 when concentrations ranged from 9 nM to 33 nM with more enriched δ^{13}C-CH_4 values (−44.6‰ to −50.6‰). Shifts in salinity across this halocline occurred within a 24 cm transition zone at approximately 19.80 m water depth in January 2015 (Fig. 5a) and within a 36 cm zone at approximately 20.0 m in January 2016 (Fig. 5b). Salinity varied from oligohaline (3.17 psu) to polyhaline (29.73 psu) across the 25 cm mini-OPP profile (Fig. 5c).

Across all profiles at the two haloclines, endmember salinity and sulfate values were in agreement with previous measurements using other sampling techniques (Brankovits et al., 2018; Brankovits et al., 2017), suggesting the records captured the full range of salinity in the flooded cave conduits. The sulfate concentrations measured here (0.1 to 28.9 mM) were also in agreement with previously reported values from this site (Brankovits et al., 2017). Sulfate to chloride ratios (SO_4^{2-}:Cl^-) were more similar to the nearby coastal sea value (0.0515) (Gondwe et al., 2010; Perry et al., 2002; Pohlman and Brankovits, 2017) than other settings in the Yucatán region (Gondwe et al., 2010; Perry et al., 2002). The highest SO_4^{2-}:Cl^- values (as high as 0.064) and highest degree of deviation from the seawater were observed in the BW. By contrast, the FW had the lowest SO_4^{2-}:Cl^- values (as low as 0.030), but these ratios were still in closer agreement with the seawater value than those in the BW. The SG SO_4^{2-}:Cl^- ratios were indistinguishable from the coastal seawater (Fig. 5). All geochemical data are available in the Appendix (Supplementary Data).

Conservative mixing and kinetic isotope models

The deviation between the conservative mixing model results with the measured values across the low-salinity-halocline reveals that a methane removal process imparting positive isotopic fractionation on the residual methane was active (Fig. 6a-b). According to the mass balance calculations, 98.9% (or ~6,560 nM) of the methane was consumed within the low-salinity-halocline in January 2015, and 98.8% (or ~3,100 nM) in the January 2016. Despite different halocline depths and thicknesses for the two sampling events, the percent removal of methane within the interface was similar. By contrast, there was no evidence of methane oxidation within the high-salinity-halocline (Fig. 6a-b).

Our data more accurately matched the closed-system Rayleigh model than the open-system model (Fig. 7), indicating that microbial methane oxidation within the gradient zone is the primary process affecting the $\delta^{13}C\text{-}CH_4$ values. Based on the Rayleigh model, microbial methane oxidation removed up to ~99.0% (or ~7,700 nM) of the methane source based on the January 2015 OPP profile, up to ~99.1% (or ~4,300 nM) according to the January 2016 OPP profile, which agrees well with the removal calculated by the mass balance approach using the conservative mixing model.

DISCUSSION

Pristine, cm-scale vertical sampling of salinity/density interfaces within flooded cave passages provides valuable details about the distribution and reactivity of methane within karst subterranean estuaries. The shallow halocline between low salinity water masses (low-salinity-halocline) plays a more significant role in methane-related biogeochemical processes than the deeper halocline associated with the low- to high-salinity gradient (high-salinity-halocline). These observations explain why manual sampling along m-scale vertical profiles did not constrain the specific location where methane oxidation occurs in this KSE (Brankovits et al., 2017). Our analysis of methane concentrations and their $\delta^{13}C$ values along salinity gradients, using mixing models and kinetic isotope models, identifies (1) a generally uniform source of methane that

343 originates from the degradation of organic matter in the overlying forest soil and (2) a
344 hotspot of methane oxidation at the shallow low-salinity-halocline where anoxic fresh
345 water and hypoxic brackish water intersect.
346
347 *Halocline dynamics affect chemical gradients*
348 Consistent with meromictic conditions for this KSE (Beddows et al., 2007;
349 Brankovits et al., 2017), low-salinity- and high-salinity-haloclines were observed in the
350 2015 and 2016 sampling events (Fig. 1b), but show distinct differences with respect to
351 their structure and position in the water column. In January 2015, the thickness of
352 shallow and deep haloclines were at least 12 cm less than in 2016, suggesting more
353 stable conditions and less mixing in 2015. Also, the average approximate water depth of
354 the low-salinity-halocline was ~40 cm deeper and the high-salinity-halocline was ~14
355 cm deeper during 2016 than in 2015, implying that the high groundwater level is
356 associated with greater mixing. These observations are consistent with a previous study
357 that found high precipitation prior to the 2016 sampling was associated with increased
358 hydraulic head and groundwater flow, which enhances mixing (Brankovits et al., 2018).
359 Indeed, the total precipitation during a 15-day time period preceding the sampling event
360 was 39 mm in 2015 and 253 mm in 2016 (Brankovits et al., 2018). Temporal and spatial
361 differences in precipitation patterns have a direct impact on the dynamic hydrology of
362 karst aquifers which directly affects mixing on recent (Kovacs et al., 2017) and paleo
363 timescales (Curtis et al., 1996; van Hengstum et al., 2010).
364 Sulfate to chloride ratios in close agreement with reported seawater values
365 (0.0515) (Gondwe et al., 2010; Perry et al., 2002; Pohlman, 2017) are found throughout
366 all profiles, which implies a marine origin for these chemical species in the KSE and
367 suggests that physical mixing of fresh and marine-derived saline waters affects all three
368 water layers. However, deviation from the regional seawater SO_4^{2-}:Cl^- value suggests
369 that additional physical or biogeochemical processes are likely to affect sulfate
370 concentrations as well. For example, lowest SO_4^{2-}:Cl^- value (0.030) observed at the
371 shallow halocline in 2015 (Fig. 4) is consistent with sulfate reduction. By contrast,

highest SO_4^{2-}:Cl^- values (as high as 0.064) and highest degree of deviation from the seawater value were observed along the deep halocline (Fig. 5) implying an additional sulfate input, possibly from gypsum/anhydrite dissolution in the interior of the Yucatán platform (Perry et al., 2002).

Profiles across the low-salinity and high-salinity-haloclines show different trends in methane concentrations and their $\delta^{13}C$ values. Methane source concentrations in the FW were higher in 2015 relative to those in 2016, but showed no substantial difference between source $\delta^{13}C$ values (as low as −67.51‰ in 2015 and −67.47‰ in 2016), indicating that methane accumulation was higher in 2015 than in 2016. Increased mixing, as discussed above, might also result in lower methane accumulation in the system. The low-salinity-halocline corresponds with an extreme shift from high to low methane concentrations, with a range between 7,793 nM (FW) to 72 nM (BW) in 2015 and between 4,325 nM (FW) to 37 nM (BW) in 2016. This reduction is associated with a substantial enrichment of $\delta^{13}C$-CH_4 from −67.5‰ (FW) to −47.8‰ (BW) in 2015 and from −67.5‰ (FW) to −55.3‰ (BW) in 2016. The pattern of increasing $\delta^{13}C$-CH_4 values across the low-salinity-halocline is a methane oxidation effect by either anaerobic or aerobic methanotrophs (e.g., Barker and Fritz, 1981; Whiticar, 1999).

The presence of relatively high dissolved oxygen in the BW during 2015 (Fig. 1d) and other sampling campaigns (Brankovits et al., 2017) would suggest the thermodynamically-favorable aerobic methane oxidation pathway is the most likely biological removal mechanism during this period (e.g., Whiticar, 1999). Although dissolved oxygen content was considerably lower in the BW during January 2016 (0-10 µM) (Fig. 1b), coastal sea studies have shown that aerobic methane oxidation is possible under these conditions (Steinle et al., 2017). Nevertheless, the low SO_4^{2-}:Cl^- value (0.030) observed at the shallow halocline in 2015 (Fig. 4) is consistent with localized sulfate reduction proximal to where methane is consumed, raising the possibility that anaerobic oxidation of methane, in addition to aerobic methanotrophy (Brankovits et al., 2017), may be active within the caves.

In contrast to the shallow profiles, the deeper high-salinity-halocline is associated with no significant trends in methane-related chemical constituents (Fig. 5). Higher methane concentrations in 2015 than in 2016 at the high-salinity-halocline imply that periods of greater methane accumulation in the FW source regime (2015 on Fig. 4) are associated with higher residual methane concentrations in deeper waters. Thus, physical mixing is most likely the key factor affecting the distribution of methane-related chemical properties across the deep interface.

Multi-model approach confirms methanotrophy

The concentration-based conservative mixing model (Fig. 6a) further indicates that the observed reduction in methane concentrations at the low-salinity-halocline was affected by methane removal; not only the physical mixing of low and high salinity waters. The extreme shift in $\delta^{13}C\text{-}CH_4$ values for the isotopic mixing model (Fig. 6b) strongly suggests the reduction of methane across this interface is coupled with isotopic fractionation that occurs during microbial methane oxidation (Barker and Fritz, 1981; Whiticar, 1999). High-resolution sampling of the entire salinity gradient made it possible to demonstrate that methane oxidation is occurring strictly at the low-salinity-halocline. This evidence suggests that methanotrophic bacteria responsible for recycling methane carbon into the food web in this habitat (Brankovits et al., 2017) are concentrated at this hotspot of methane oxidation. Evidence for additional input of sulfate near the high-salinity-halocline, as implied from SO_4^{2-}:Cl^- values, suggests that mixing processes are more complex in the flooded coastal caves than assumed by the conservative mixing model, which assumes the local mixing regime consists of FW and the marine-derived SG, with BW being a mixture of these endmembers. As a result, we use kinetic isotope models as an alternate approach to investigate methane oxidation dynamics across the low-salinity-halocline, where methane consumption is evident from the profiles.

A comparison of the closed- and open-system kinetic isotope models demonstrates that the measured methane concentrations and isotopic values are most similar to the values predicted by the closed-system isotope model (Fig. 7). This

observation provides additional, robust evidence that the variability in measured methane isotopic ratios is primarily due to microbial oxidation, with minimal influence by mixing and external inputs, and that the methane originates from a generally uniform source. Considering the strictly anoxic conditions required for the production of methane with a source $\delta^{13}C$ signature as low as −67.5‰, we conclude that methane production takes place in the anoxic saturated soil/rock-matrix overlying the cave passages. The downward migration of methane from nearby soils is consistent with the distribution of terrestrial origin ($\delta^{13}C$ = −28.0‰) dissolved organic carbon in this environment (Brankovits et al., 2017).

Assuming the lowest measured $\delta^{13}C$-CH_4 value (R_0 = −67.5‰) is the source signature, and using the isotope fractionation factor determined by the Rayleigh model, it was possible to estimate the corresponding FW endmember concentration for each measured methane concentration value from the low-salinity-halocline profiles. These calculations predict the average source methane concentrations were ~8,700 nM in 2015 and ~5,200 nM in 2016. The difference between the calculated endmember methane concentrations for the two sampling periods is consistent with there being higher methane accumulation in 2015 than 2016. Methanotrophy, however, removed a similar fraction of methane originating from the FW in both years. The closed-system kinetic isotope model and the mass balance calculations based on a conservative mixing model agree that at least 98% of available methane was oxidized during both years, suggesting that microbial methane oxidation is an efficient methane sink in KSE cave passages.

Conclusions

Methane released from anoxic soil/rock-matrix into the flooded cave network is consumed in the shallow portion of the meteoric lens at a 12 - 24 cm thick halocline located between low-salinity water masses within the studied karst subterranean estuary. By contrast, we observed no evidence of methane oxidation at the deeper halocline between the meteoric lens and the saline groundwater. Mixing models and the kinetic isotope models provide evidence for efficient removal (at least 98%) of methane present

458 in the cave environment by microbial methane oxidation in both sampling years. This
459 observation contributes to the growing evidence that subterranean estuaries have a role
460 in greenhouse gas dynamics (Pain et al., 2019) and act as a methane sink (Brankovits et
461 al., 2018; Schutte et al., 2016), which affects the amount and type of greenhouse gases
462 and organic matter emitted into the coastal ocean by submarine groundwater discharge.
463 Biogeochemical processes transforming organic matter in the cave environment within
464 KSEs are particularly important because the vast networks of natural conduits provide
465 direct pathway of terrestrial materials into the coastal sea (Gonneea et al., 2014; Young
466 et al., 2008). Moreover, our findings demonstrate that cave environments in the phreatic
467 zone of a karst system are capable of acting as a methane sink, similar to air-filled caves
468 in the vadose zone (Fernandez-Cortes et al., 2015; Ojeda et al., 2019; Webster et al.,
469 2018). Such increasing collective evidence for methane consumption in a globally
470 distributed environment should encourage future research in karst systems that may have
471 a greater role in greenhouse gas dynamics than previously thought.
472 Differences in measured concentrations and $\delta^{13}C$ ratios of methane, and in
473 calculated initial methane source concentrations indicate slightly more efficient methane
474 accumulation in the flooded cave environment during the 2015 sampling period than in
475 2016. These temporal changes in methane dynamics are consistent with matching time-
476 series of methane concentrations and hydrologic parameters from a related study
477 (Brankovits et al., 2018). Moreover, the same time-series suggest that the observed
478 patterns in halocline dynamics in this study (e.g., vertically thicker salinity gradient in
479 2016) based on coupled sulfate and salinity profiles (Fig. 4-5) are a result of
480 precipitation-induced hydrologic processes, such as an increase in the hydraulic head
481 and flow velocity. For all these reasons, we conclude that hydrologically driven
482 halocline dynamics impact the biogeochemical cycling of carbon in KSEs. These
483 findings provide new insight into organic matter transformation and greenhouse gas
484 dynamics in KSEs prior to material transport to the coastal ocean. Considering that
485 methane provides carbon and energy for the food web in a variety of aquatic settings
486 (Bastviken et al., 2003; He et al., 2015) and the current study site (Brankovits et al.,

2017), the above findings also contribute to the understanding of how anchialine ecosystems function within subterranean estuaries.

To expand our current understanding of organic matter transformation and methane dynamics in KSEs, future studies should focus on: (1) quantifying the upside-down methane flux; (2) exploring the temporal constraints of dissolved oxygen dynamics and the potential balance between aerobic and anaerobic methane oxidation; (3) determining linkages between halocline dynamics and biogeochemical processes, including the elemental cycling of carbon, nitrogen and sulfur; (4) characterizing the microbiological communities associated with the highly structured environmental gradients in the water column; and (5) testing how regional variation affects the above listed processes on the landscape-level.

ACKNOWLEDGEMENTS

Funding for D.B. was provided by the Research-in-Residence program (NSF award #1137336, Inter-university Training in Continental-scale Ecology), the Boost Fellowship (Texas A&M University at Galveston) and the joint Postdoctoral Scholar Program by Woods Hole Oceanographic Institution and U.S. Geological Survey. We express our gratitude to Michael Casso (USGS) and Emile Bergeron (USGS) for their help with developing the OctoPiPi water sampler. Sean P. Sylva helped with laboratory analyses. We thank Jacob Pohlman, Jake Emmert and István Brankovits for assistance with field expeditions, and Moody Gardens (Galveston, Texas) for supporting the fieldwork. Special thanks to the late Bil Phillips (Speleotech) for helping our field operations in Mexico. Any use of trade names is for descriptive purposes and does not imply endorsement by the U.S. government. All data from this study are available as Supplementary Data.

APPENDIX: SUPPLEMENTARY DATA

Supplementary data associated with this article can be found in the online version.

515 **REFERENCES**

516 Alvarez, F., Iliffe, T.M., Benitez, S., Brankovits, D. and Villalobos, J.L. (2015) New
517 records of anchialine fauna from the Yucatan Peninsula, Mexico. *Check List* **11**, 1505.

518 Barker, J.F. and Fritz, P. (1981) Carbon isotope fractionation during microbial methane
519 oxidation. *Nature* **293**, 289-291.

520 Bastviken, D., Cole, J., Pace, M. and Tranvik, L. (2004) Methane emissions from lakes:
521 Dependence of lake characteristics, two regional assessments, and a global estimate.
522 *Global Biogeochemical Cycles* **18**.

523 Bastviken, D., Cole, J.J., Pace, M.L. and Van de Bogert, M.C. (2008) Fates of methane
524 from different lake habitats: Connecting whole-lake budgets and CH4 emissions.
525 *Journal of Geophysical Research: Biogeosciences* **113**.

526 Bastviken, D., Ejlertsson, J., Sundh, I. and Tranvik, L. (2003) Methane as a source of
527 carbon and energy for lake pelagic food webs. *Ecology* **84**, 969-981.

528 Bastviken, D., Tranvik, L.J., Downing, J.A., Crill, P.M. and Enrich-Prast, A. (2011)
529 Freshwater methane emissions offset the continental carbon sink. *Science* **331**, 50-50.

530 Bauer-Gottwein, P., Gondwe, B.R., Charvet, G., Marín, L.E., Rebolledo-Vieyra, M. and
531 Merediz-Alonso, G. (2011) the Yucatán Peninsula karst aquifer, Mexico. *Hydrogeology*
532 *Journal* **19**, 507-524.

533 Beck, A.J., Charette, M.A., Cochran, J.K., Gonneea, M.E. and Peucker-Ehrenbrink, B.
534 (2013) Dissolved strontium in the subterranean estuary - Implications for the marine
535 strontium isotope budget. *Geochimica et Cosmochimica Acta* **117**, 33-52.

536 Beddows, P., Smart, P., Whitaker, F. and Smith, S. (2002) Density stratified
537 groundwater circulation on the Caribbean Coast of the Yucatan Peninsula, Mexico. Karst
538 Frontiers. *Karst Waters Institute Special Publication* **7**, 129-134.

539 Beddows, P.A., Smart, P.L., Whitaker, F.F. and Smith, S.L. (2007) Decoupled fresh-
540 saline groundwater circulation of a coastal carbonate aquifer: Spatial patterns of
541 temperature and specific electrical conductivity. *Journal of Hydrology* **346**, 18-32.

542 Bishop, R.E., Humphreys, W.F., Cukrov, N., Zic, V., Boxshall, G.A., Cukrov, M., Iliffe,
543 T.M., Krsinic, F., Moore, W.S., Pohlman, J.W. and Sket, B. (2015) 'Anchialine'
544 redefined as a subterranenan estuary in crevicular or cavernous geological setting.
545 *Journal of Crustacean Biology* **35**, 511-514.

546 Boetius, A. and Wenzhofer, F. (2013) Seafloor oxygen consumption fuelled by methane
547 from cold seeps. *Nature Geoscience* **6**, 725-734.

548 Brankovits, D., Pohlman, J., Ganju, N.K., Iliffe, T., Lowell, N., Roth, E., Sylva, S.,
549 Emmert, J. and Lapham, L. (2018) Hydrologic controls of methane dynamics in karst
550 subterranean estuaries. *Global Biogeochemical Cycles* **32**, 1759-1775.

551 Brankovits, D., Pohlman, J.W., Niemann, H., Leigh, M.B., Leewis, M.-C., Becker,
552 K.W., Iliffe, T.M., Alvarez, F., Lehmann, M.F. and Phillips, B. (2017) Methane-and
553 dissolved organic carbon-fueled microbial loop supports a tropical subterranean estuary
554 ecosystem. *Nature Communications* **8**, 1835.

555 Chanton, J.P. and Lewis, F.G. (1999) Plankton and dissolved inorganic carbon isotopic
556 composition in a river-dominated estuary: Apalachicola Bay, Florida. *Estuaries* **22**, 575-
557 583.

558 Corliss, J.B., Dymond, J., Gordon, L.I., Edmond, J.M., Herzen, R.P.V., Ballard, R.D.,
559 Green, K., Williams, D., Bainbridge, A., Crane, K. and Vanandel, T.H. (1979)
560 Submarine thermal springs on the Galapagos Rift. *Science* **203**, 1073-1083.

561 Coutino, A., Stastna, M., Kovacs, S. and Reinhardt, E. (2017) Hurricanes Ingrid and
562 Manuel (2013) and their impact on the salinity of the Meteoric Water Mass, Quintana
563 Roo, Mexico. *Journal of Hydrology* **551**, 715-729.

564 Curtis, J.H., Hodell, D.A. and Brenner, M. (1996) Climate variability on the Yucatan
565 Peninsula (Mexico) during the past 3500 years, and implications for Maya cultural
566 evolution. *Quaternary Research* **46**, 37-47.

567 Damm, E., Schauer, U., Rudels, B. and Haas, C. (2007) Excess of bottom-released
568 methane in an Arctic shelf sea polynya in winter. *Continental Shelf Research* **27**, 1692-
569 1701.

570 Deines, P., Wooller, M.J. and Grey, J. (2009) Unravelling complexities in benthic food
571 webs using a dual stable isotope (hydrogen and carbon) approach. *Freshwater Biology*
572 **54**, 2243-2251.

573 DelVecchia, A.G., Stanford, J.A. and Xu, X. (2016) Ancient and methane-derived
574 carbon subsidizes contemporary food webs. *Nature Communications* **7**, 13163.

575 Devlin, S.P., Saarenheimo, J., Syväranta, J. and Jones, R.I. (2015) Top consumer
576 abundance influences lake methane efflux. *Nature Communications* **6**, 8787.

577 Fernandez-Cortes, A., Cuezva, S., Alvarez-Gallego, M., Garcia-Anton, E., Pla, C.,
578 Benavente, D., Jurado, V., Saiz-Jimenez, C. and Sanchez-Moral, S. (2015) Subterranean
579 atmospheres may act as daily methane sinks. *Nature Communications* **6**, 7003.

580 Ford, D. and Williams, P.D. (2013) *Karst Hydrogeology and Geomorphology*. John
581 Wiley & Sons, West Sussex.

582 Gondwe, B.R., Lerer, S., Stisen, S., Marín, L., Rebolledo-Vieyra, M., Merediz-Alonso,
583 G. and Bauer-Gottwein, P. (2010) Hydrogeology of the south-eastern Yucatan
584 Peninsula: new insights from water level measurements, geochemistry, geophysics and
585 remote sensing. *Journal of Hydrology* **389**, 1-17.

586 Gonneea, M.E., Charette, M.A., Liu, Q., Herrera-Silveira, J.A. and Morales-Ojeda, S.M.
587 (2014) Trace element geochemistry of groundwater in a karst subterranean estuary
588 (Yucatan Peninsula, Mexico). *Geochimica et Cosmochimica Acta* **132**, 31-49.

589 Grey, J. (2016) The incredible lightness of being methane-fuelled: stable isotopes reveal
590 alternative energy pathways in aquatic ecosystems and beyond. *Frontiers in Ecology and*
591 *Evolution* **4,** 8.

592 He, R., Wooller, M.J., Pohlman, J.W., Tiedje, J.M. and Leigh, M.B. (2015) Methane-
593 derived carbon flow through microbial communities in arctic lake sediments.
594 *Environmental Microbiology* **17**, 3233-3250.

595 Humphreys, W. (1999) Physico-chemical profile and energy fixation in Bundera
596 Sinkhole, an anchialine remiped habitat in north-western Australia. *Journal of the Royal*
597 *Society of Western Australia* **82**, 89-98.

598 Iliffe, T.M. and Kornicker, L.S. (2009) Worldwide diving discoveries of living fossil
599 animals from the depths of anchialine and marine caves. Smithsonian Contributions to
600 Marine Sciences 38, 269-280.

601 IPCC (2014) *Climate Change 2014–Impacts, Adaptation and Vulnerability: Regional*
602 *Aspects*. Cambridge University Press.

603 Kambesis, P.N. and Coke, J.G. (2013) *Overview of the controls on eogenetic cave and*
604 *karst development in Quintana Roo, Mexico, Coastal Karst Landforms*. Springer, pp.
605 347-373.

606 Kessler, J., Reeburgh, W. and Tyler, S. (2006) Controls on methane concentration and
607 stable isotope (δ2H-CH4 and δ13C-CH4) distributions in the water columns of the Black
608 Sea and Cariaco Basin. *Global Biogeochemical Cycles* **20**.

609 Kottek, M., Grieser, J., Beck, C., Rudolf, B. and Rubel, F. (2006) World map of the
610 Köppen-Geiger climate classification updated. *Meteorologische Zeitschrift* **15**, 259-263.

611 Kovacs, S.E., Reinhardt, E.G., Stastna, M., Coutino, A., Werner, C., Collins, S.V.,
612 Devos, F. and Le Maillot, C. (2017) Hurricane Ingrid and Tropical Storm Hanna's
613 effects on the salinity of the coastal aquifer, Quintana Roo, Mexico. *Journal of*
614 *Hydrology* **551**, 703-714.

615 Kroeger, K. and Charette, M. (2008) Nitrogen biogeochemistry of submarine
616 groundwater discharge. *Limnology and Oceanography* **53**, 1025-1039.

617 Kwon, E.Y., Kim, G., Primeau, F., Moore, W.S., Cho, H.M., DeVries, T., Sarmiento,
618 J.L., Charette, M.A. and Cho, Y.K. (2014) Global estimate of submarine groundwater
619 discharge based on an observationally constrained radium isotope model. *Geophysical*
620 *Research Letters* **41**, 8438-8444.

621 Leonte, M., Kessler, J.D., Kellermann, M.Y., Arrington, E.C., Valentine, D.L. and
622 Sylva, S.P. (2017) Rapid rates of aerobic methane oxidation at the feather edge of gas
623 hydrate stability in the waters of Hudson Canyon, US Atlantic Margin. *Geochimica et*
624 *Cosmochimica Acta* **204**, 375-387.

625 Levin, L.A. (2005) Ecology of cold seep sediments: interactions of fauna with flow,
626 chemistry and microbes. *Oceanography and Marine Biology: An Annual Review* **43**, 1-
627 46.

628 Magen, C., Lapham, L.L., Pohlman, J.W., Marshall, K., Bosman, S., Casso, M. and
629 Chanton, J.P. (2014) A simple headspace equilibration method for measuring dissolved
630 methane. *Limnology and Oceanogaphy: Methods* **12**, 637-650.

631 Menning, D.M., Wynn, J.G. and Garey, J.R. (2015) Karst estuaries are governed by
632 interactions between inland hydrological conditions and sea level. *Journal of Hydrology*
633 **527**, 718-733.

634 Moore, W.S. (2010) The effect of submarine groundwater discharge on the ocean.
635 *Annual Review of Marine Science* **2**, 59-88.

636 Ojeda, L., Vadillo, I., Etiope, G., Benavente, J., Liñán, C., del Rosal, Y., Tapia, S.T.,
637 Moríñigo, M.Á. and Carrasco, F. (2019) Methane sources and sinks in karst systems: the
638 Nerja cave and its vadose environment (Spain). *Geochimica et Cosmochimica Acta* **259**,
639 302-315.

640 Pain, A.J., Martin, J.B. and Young, C.R. (2019) Sources and sinks of CO2 and CH4 in
641 siliciclastic subterranean estuaries. *Limnology and Oceanography* **64**, 1500-1514.

642 Paull, C.K., Hecker, B., Commeau, R., Freemanlynde, R.P., Neumann, C., Corso, W.P.,
643 Golubic, S., Hook, J.E., Sikes, E. and Curray, J. (1984) Biological communities at the
644 Florida escarpment resemble hydrothermal vent taxa. *Science* **226**, 965-967.

645 Perry, E., Velazquez-Oliman, G. and Marin, L. (2002) The hydrogeochemistry of the
646 karst aquifer system of the northern Yucatan Peninsula, Mexico. *International Geology*
647 *Review* **44**, 191-221.

Pohlman, J.W. (2011) The biogeochemistry of anchialine caves: progress and possibilities. *Hydrobiologia* **677**, 33-51.

Pohlman, J.W., and Brankovits, D. (2017) Water column physical and chemical properties of Cenote Bang, a component of the Ox Bel Ha cave network within the subterranean estuary coastal aquifer of the Yucatan Peninsula, from December 2013 to January 2016. *U.S. Geological Survey data release*, https://doi.org/10.5066/F7DJ5DJW.

Pohlman, J.W., Ruppel, C., Hutchinson, D.R., Downer, R. and Coffin, R.B. (2008) Assessing sulfate reduction and methane cycling in a high salinity pore water system in the northern Gulf of Mexico. *Marine and Petroleum Geology* **25**, 942-951.

Popp, B.N., Sansone, F.J., Rust, T.M. and Merritt, D.A. (1995) Determination of concentration and carbon isotopic composition of dissolved methane in sediments and nearshore waters. *Analytical Chemistry* **67**, 405-411.

Reeburgh, W.S. (2007) Oceanic methane biogeochemistry. *Chemical Reviews* **107**, 486-513.

Santoro, A.E. (2010) Microbial nitrogen cycling at the saltwater-freshwater interface. *Hydrogeology Journal* **18**, 187-202.

Santoro, A.E., Francis, C.A., de Sieyes, N.R. and Boehm, A.B. (2008) Shifts in the relative abundance of ammonia-oxidizing bacteria and archaea across physicochemical gradients in a subterranean estuary. *Environmental Microbiology* **10**, 1068-1079.

Schutte, C.A., Wilson, A.M., Evans, T., Moore, W.S. and Joye, S.B. (2016) Methanotrophy controls groundwater methane export from a barrier island. *Geochimica et Cosmochimica Acta* **179**, 242-256.

Seymour, J., Humphreys, W. and Mitchell, J. (2007) Stratification of the microbial community inhabiting an anchialine sinkhole. *Aquatic Microbial Ecology* **50**, 11-24.

Socki, R.A., Perry, E.C. and Romanek, C.S. (2002) Stable isotope systematics of two cenotes from the northern Yucatan Peninsula, Mexico. *Limnology and Oceanography* **47**, 1808-1818.

Steinle, L., Maltby, J., Treude, T., Kock, A., Bange, H.W., Engbersen, N., Zopfi, J., Lehmann, M.F. and Niemann, H. (2017) Effects of low oxygen concentrations on aerobic methane oxidation in seasonally hypoxic coastal waters. *Biogeosciences* **14**, 1631-1645.

Stock, J.H., Iliffe, T.M. and Williams, D. (1986) The concept of anchialine reconsidered. *Stygologia* **2**, 90-92.

van Hengstum, P.J., Reinhardt, E.G., Beddows, P.A. and Gabriel, J.J. (2010) Linkages between Holocene paleoclimate and paleohydrogeology preserved in a Yucatan underwater cave. *Quaternary Science Reviews* **29**, 2788-2798.

van Hengstum, P.J., Scott, D.B., Grocke, D.R. and Charette, M.A. (2011) Sea level controls sedimentation and environments in coastal caves and sinkholes. *Marine Geology* **286**, 35-50.

Webster, K.D., Drobniak, A., Etiope, G., Mastalerz, M., Sauer, P.E. and Schimmelmann, A. (2018) Subterranean karst environments as a global sink for atmospheric methane. *Earth and Planetary Science Letters* **485**, 9-18.

Wetzel, R.G. (2001) *Limnology: Lake and River Ecosystems*. Gulf Professional Publishing.

Whiticar, M.J. (1999) Carbon and hydrogen isotope systematics of bacterial formation and oxidation of methane. *Chemical Geology* **161**, 291-314.

Young, M.B., Gonneea, M.E., Fong, D.A., Moore, W.S., Herrera-Silveira, J. and Paytan, A. (2008) Characterizing sources of groundwater to a tropical coastal lagoon in a karstic area using radium isotopes and water chemistry. *Marine Chemistry* **109**, 377-394.

697 **Figures and Captions**

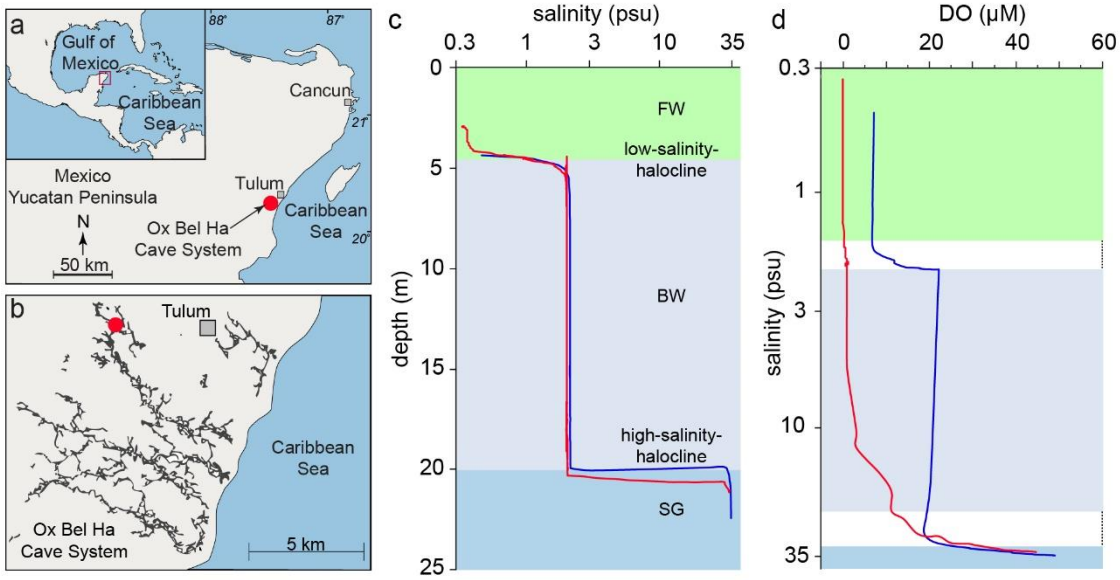

698

699 Figure 1: Field site and general vertical structure of the water column in a cave passage
700 flooded by the subterranean estuary. (a) The study site is in the Yucatán Peninsula,
701 Mexico. (b) Map of Ox Bel Ha Cave System showing explored cave passages that
702 provide access to the subterranean estuary. The study site (red dot) is located 6.6 km
703 inland from the coast. Physicochemical profiles obtained with a multi-parameter data
704 sonde in January 2015 (blue line) and January 2016 (red line) as part of a preceding
705 study (Brankovits et al., 2017) show (c) increasing salinity along a depth profile, as well
706 as (d) increasing dissolved oxygen (DO) concentrations with increasing salinity (and
707 depth). A shallow, low-salinity-halocline within the meteoric water layer separates the
708 anoxic meteoric fresh water (FW) from the meteoric brackish water (BW). The deeper,
709 high-salinity-halocline separates the meteoric lens from the saline groundwater (SG).

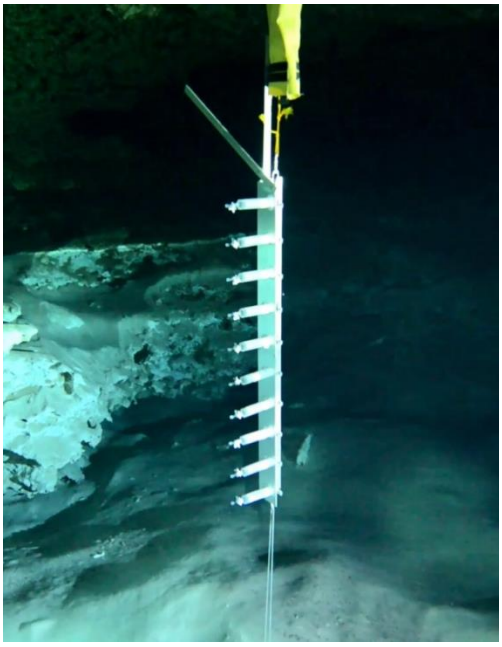

Figure 2: The OctoPiPi (OPP) deployed for sample collection in the water column of a flooded cave passage. The OPP contains ten 60 ml syringes that are distributed 12 cm vertically from each other. A smaller mini-OPP, which contained ten 60 ml syringes distributed 2.5 cm from each other, required a similar deployment procedure.

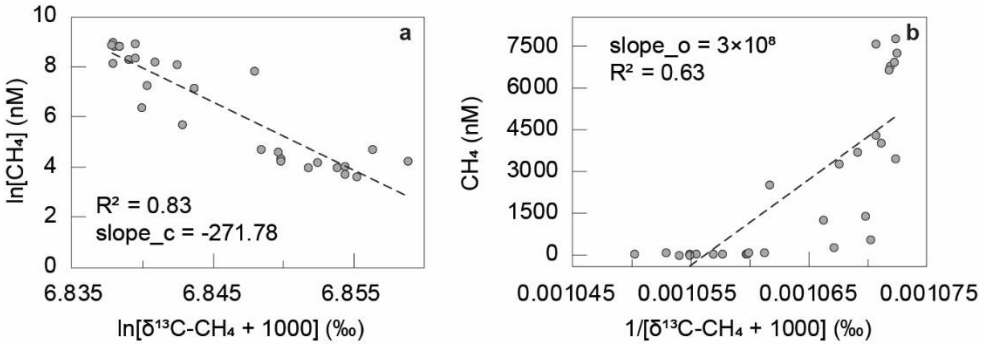

Figure 3: Methane concentration values plotted with values derived from the $\delta^{13}C$-CH_4 ratios for the (A) Rayleigh and (B) open-system models. The slopes of the linear regressions were used to calculate the fractionation factor (α) for the Rayleigh and open-system kinetic isotope models.

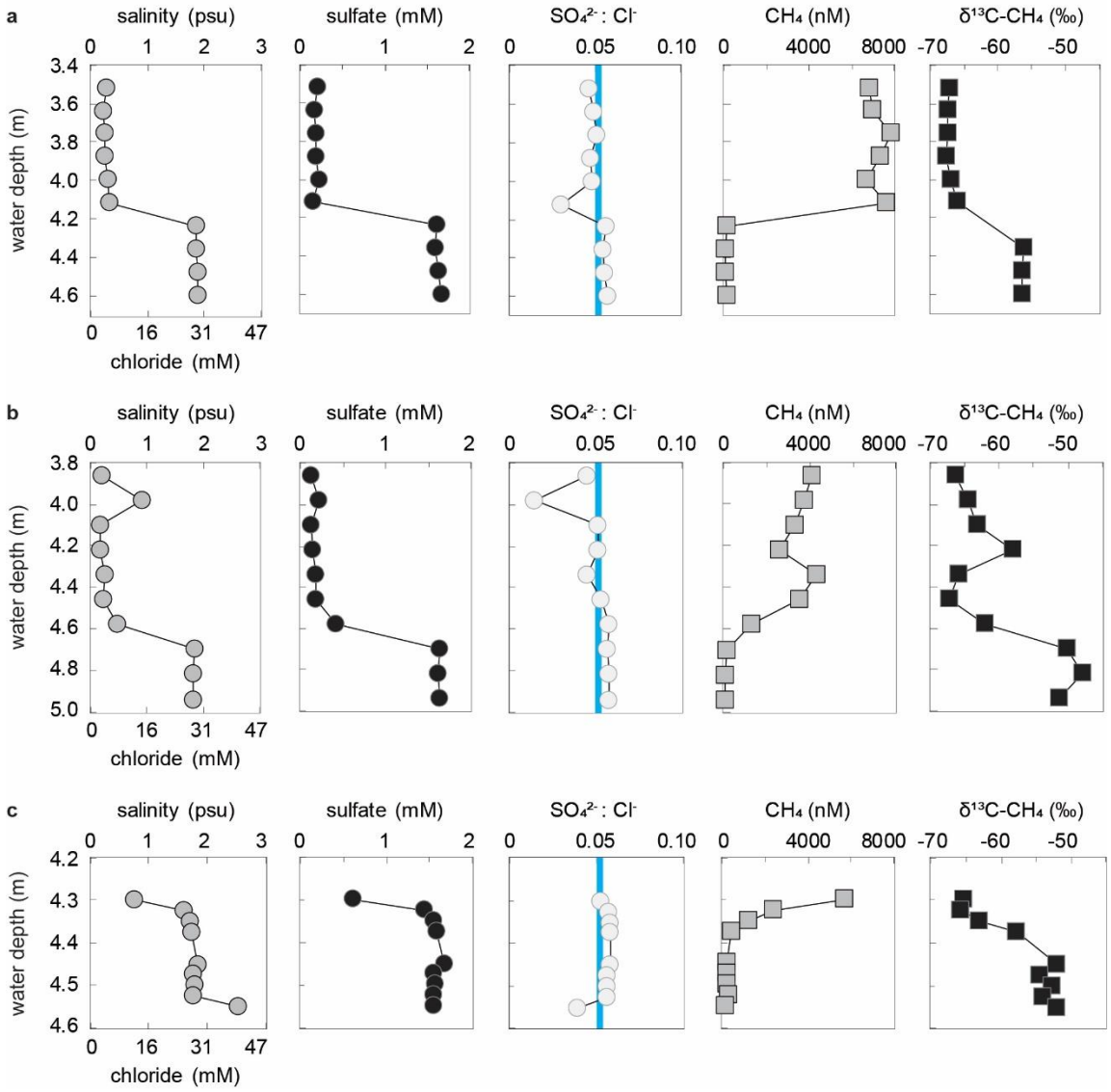

Figure 4: High-resolution depth profiles of chemical constituents across the low-salinity-halocline between the fresh water (FW) and brackish water (BW) layers. Samples were collected with the OPP in (a) January 2015 and (b) January 2016, as well as with the mini-OPP (c) in January 2016. Symbols of individual data points contain the analytical uncertainty (std. dev.) of the measured values. The blue line is the SO_4^{2-}:Cl^- ratio (0.0515) of the regional seawater.

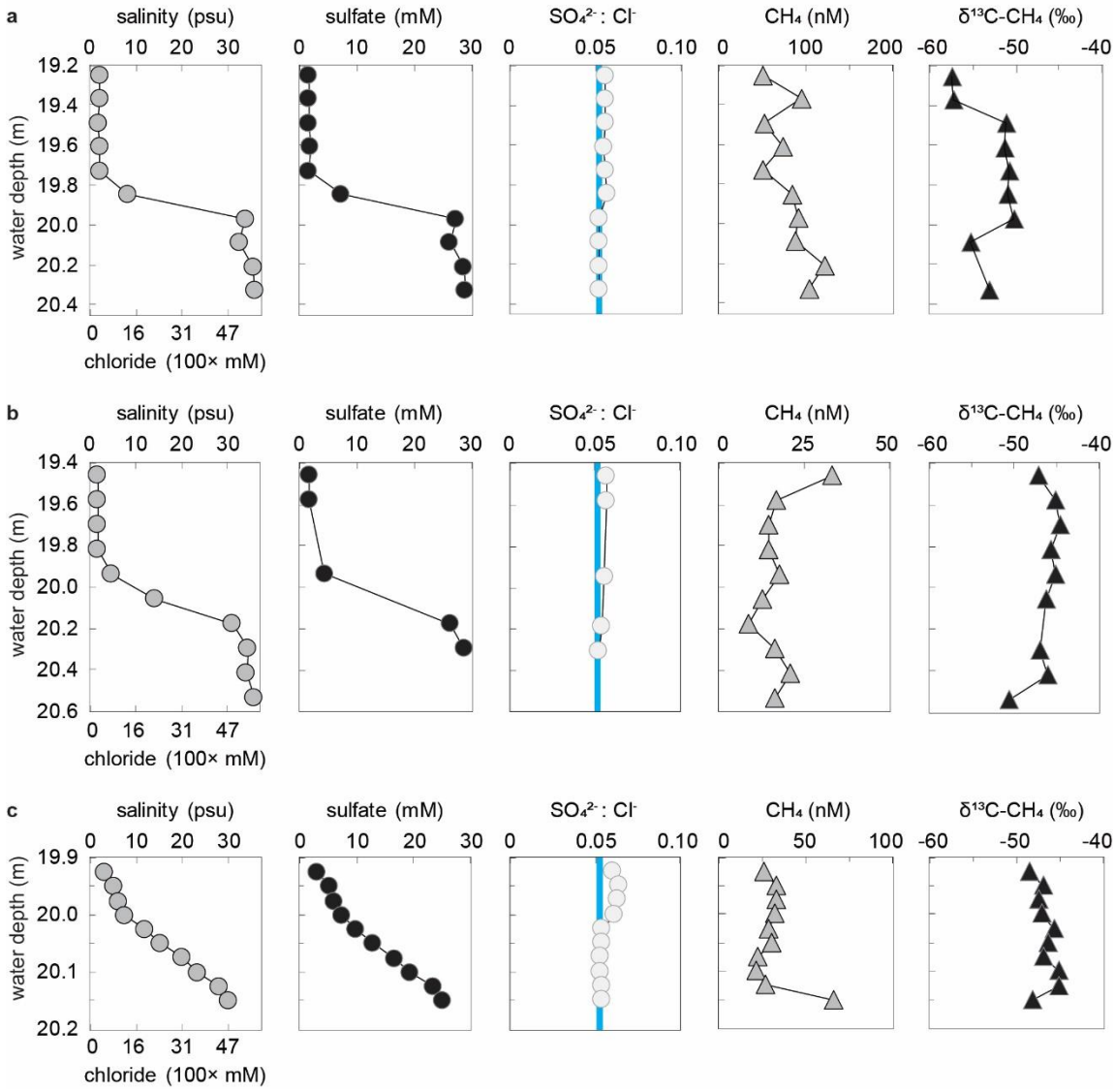

Figure 5: High-resolution depth profiles of chemical constituents across the high-salinity-halocline between the brackish water (BW) and saline groundwater (SG). Samples were collected with the OPP in (a) January 2015 and (b) January 2016, as well as with the mini-OPP (c) in January 2016. Symbols of individual data points contain the analytical uncertainty (std. dev.) of the measured values. The blue line is the SO_4^{2-}:Cl^- ratio (0.0515) of the regional seawater.

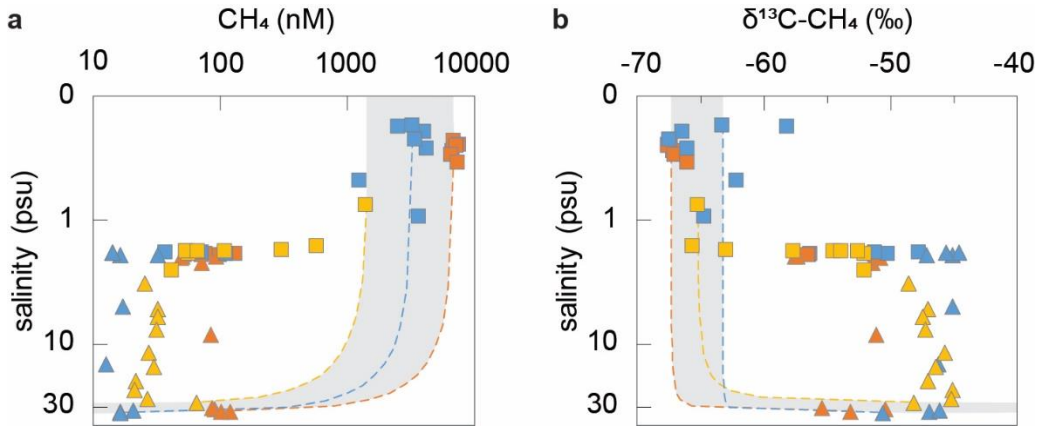

Figure 6: Salinity-property plots and the conservative mixing model output. (a) Salinity and methane concentrations plotted on log-scale. (b) Salinity and δ^{13}C-CH_4 values, with salinity plotted on log-scale. Colors indicate January 2015 (orange) and January 2016 (blue) OPP-deployments, and the January 2016 (yellow) mini-OPP deployment. Samples obtained from the low-salinity-halocline indicated as squares, and samples obtained from the high-salinity-halocline indicated as triangles. Colored dotted lines are conservative mixing model results for their respective event and represent the expected distribution when there is physical mixing only (no reactions). Grey area is the total area of the conservative mixing results. Depletion of the measured constituent relative to the concentration-based model suggests consumption of methane within the salinity transition. Deviation of the δ^{13}C-CH_4 values toward more positive values within the region of consumption corroborates that methane oxidation was active. Symbol of individual data points contain the analytical uncertainty (std. dev,) of each measurement.

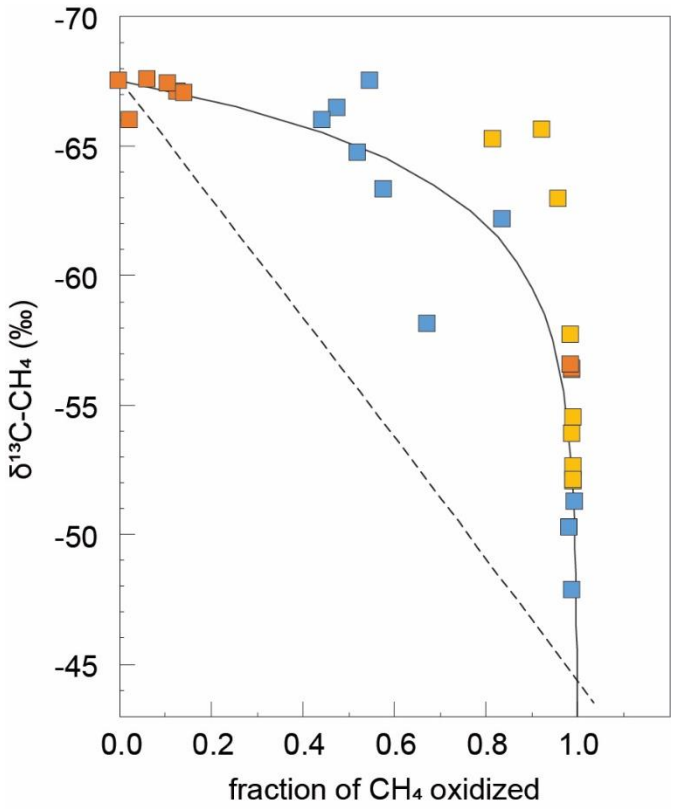

Figure 7: Measured δ^{13}C-CH_4 values plotted against the calculated fractions of methane oxidized. Colors indicate January 2015 (orange) and January 2016 (blue) OPP-deployments, and the January 2016 (yellow) mini-OPP deployment. The fraction of methane oxidized for the collected samples was calculated as $f = 1 - C/C_0$ where C is the methane concentration of each sample collected across the low-salinity-halocline and C_0 (7,544 nM) is the concentration of the unoxidized FW endmember (see methods for more details). These values are compared to model predictions from the closed-system model calculated using Eq. 1 (sold line) and the open-system calculated using Eq. 2 (dotted line) models. The closed-system model more closely matches the data than the open-system model.